

Gas-assisted discharge flow of granular media from silosY. Zhou,^{1,2,*} P.-Y. Lagrée,³ S. Popinet,³ P. Ruyer,¹ and P. Aussillous^{2,†}¹*Institut de Radioprotection et de Sûreté Nucléaire (IRSN), PSN-RES, SEMIA, LIMAR, Cadarache, Saint Paul-Lez-Durance 13115, France*²*Aix-Marseille Université, CNRS, IUSTI, Marseille 13013, France*³*Sorbonne Université, CNRS UMR 7190, Institut Jean le Rond d'Alembert, F-75005 Paris, France*

(Received 15 February 2019; published 18 December 2019)

We studied experimentally the discharge of a vertical silo filled by spherical glass beads and assisted by injection of air from the top at a constant flow rate, a situation which has practical interest for nuclear safety or air-assisted discharge of hoppers. The measured parameters are the mass flow rate and the pressure along the silo, while the controlled parameters are the size of particles and the flow rate of air. Increasing the air flow rate induces an increase in the granular media flow rate. Using a two-phase continuum model with a frictional rheology to describe particle-particle interactions, we reveal the role played by the air-pressure gradient at the orifice. Based on this observation, we propose a simple analytical model which predicts the mass flow rate of a granular media discharged from a silo with injection of gas. This model takes into account the coupling with the gas flow as well as the silo geometry, position, and size of the orifice.

DOI: [10.1103/PhysRevFluids.4.124305](https://doi.org/10.1103/PhysRevFluids.4.124305)**I. INTRODUCTION**

The flow of granular media cannot be simply described using standard fluid models, especially when coupled with the flow of an interstitial fluid. Continuum models for granular media using a specific frictional rheology are still under development. Among these models, let us consider the so-called $\mu(I)$ rheology, based on a local constitutive law relating the local shear rate and the stress tensor [1]. Using this $\mu(I)$ rheology, several flow configurations have been successfully described thanks to numerical simulation, including granular column collapse and discharge of large and narrow silos [2–6]. These flows only considered dry granular media for which interactions between the particles and the surrounding fluid can be neglected. In the present study, we consider the discharge flow of granular media from a silo assisted by injection of air from the top and we focus on the role of the gas, flowing in a moving granular medium with interactions between both phases, on the particle flow rate. We start from an experimental study in quasisteady conditions which reveals several flow regimes. We then show that this two-phase flow can be modeled using two interpenetrating continuum media: the granular medium with a frictional rheology, and a Darcy-Forchheimer flow for the gas phase, coupled through drag-related friction.

This study has been motivated by a specific case. Let us consider a hypothetical accidental scenario in nuclear power plants: following a reactivity insertion in the core of the reactor, a fuel rod can break and its contents can be ejected toward the surrounding water (at around 600 K and 15.5 MPa). Fuel rods are 4-m-long cylindrical tubes of 1 cm diameter that under some specific

*Present address: Beijing Key Laboratory of Passive Safety Technology for Nuclear Energy, North China Electric Power University, Beijing 102206, China.

†pascale.aussillous@univ-amu.fr

accidental conditions, could contain high-pressure gases (up to 100 MPa [7]) and small size (in the range of 10 to 1000 μm) fuel particles. The ejection of those high-temperature particles (up to around 2000 K) could have serious consequences for nuclear safety, in particular if the flow rate is high. The impact of the discharge of internal gases on the particles flow rate has thus to be determined. More generally, similar flow configurations also occur in processes such as air-assisted discharge of hoppers or pipe conveying.

Let us first briefly consider the discharge of a granular media out of a silo toward a larger vessel at constant pressure in the absence of any grain-fluid interaction. The steady-state flow rate is mainly determined by the size of the aperture, say D , and can be computed thanks to the Hagen-Beverloo law [8,9] (see a translation of the original article of Hagen in [8]). When the aperture is on a lateral side of a silo of width W , friction along the walls can impact the flow rate for relatively small aspect ratios W/D [6]. The size of the grain only acts as a second-order parameter: the flow rate depends on the ratio between the aperture size and the particle diameter, D/d , only for small values of this number [10–12].

Even without the net gas flow rate through the silo orifice, the interaction between gas and particles may have to be considered, with viscous friction acting as an additional drag [13]. The impact of countercurrent air flow on the discharge of silos has been studied both experimentally [14,15] and numerically using discrete models for particles [16] and is not negligible for small particles (around 100 μm for glass beads). Air-assisted discharge of hoppers has motivated several studies [17–19]. Analysis of the flows in several geometrical configurations of rather large silos leads to the evidence that the pertinent driving force for the granular flow rate through the orifice is the sum of the weight and the fluid pressure gradient along the normal to the aperture and in its vicinity. Therefore, models considering the impact of the air flow on the steady-discharge rate have been proposed that extend the Hagen-Beverloo law to those configurations, [14]. The fluid pressure gradient can be related to the fluid flow rate through the granular media thanks to classical models for flow through porous media.

Our main objective is first to assess this behavior for different silo configurations where wall friction and orifice orientation with respect to gravity are varied. Then we address the ability of a continuum model to reproduce this behavior thanks to the comparison between numerical simulation and experimental results. The article is organized as follows. We first present an experimental setup dedicated to the study of the flow of air and of a simple granular media (glass beads of uniform size d) through a silo of simple geometry with an orifice of variable size and position; see Sec. II. A two-phase continuum model is presented in Sec. III together with its numerical implementation in a simplified configuration. Based on this model, the relation between gas and granular flow rates is analyzed in Sec. IV, where an analytical model is proposed. In Sec. V, the impact of the position of the orifice is analyzed and the ability of the model to reproduce the influence of this parameter is studied.

II. EXPERIMENTAL OBSERVATIONS

A. Experimental setup

Several silos, which are air tight except at the aperture, have been built for this study by varying the shape of the tank (cylindrical and rectangular) and the position of the orifice (bottom or lateral), as can be seen in Fig. 1 and Table I.

The cylindrical hoppers consist of a smooth Perspex cylinder, whereas the rectangular hoppers have a front wall in Perspex to allow visualization and a back wall in metal. The orifice consists either of a circular hole of variable diameter D or a rectangular hole of variable dimensions $W \times D$ (where W is the silo thickness for rectangular silos or the orifice arc length for cylindrical silos). The orifice can be located at the center of the silo bottom or on the lateral wall, 20 mm above the bottom. To avoid an effect of the walls thickness, they have been bevelled along the aperture with an angle of 30° to the vertical (see [6] for more details). The typical height H of the silos is always one order of magnitude larger than its lateral extent L to prevent size effects. The top of the silo is connected to an air-injection system (density $\rho_f = 1.2 \text{ kg/m}^3$ and viscosity $\eta_f = 1.8 \times 10^{-5} \text{ Pa s}$) which provides a

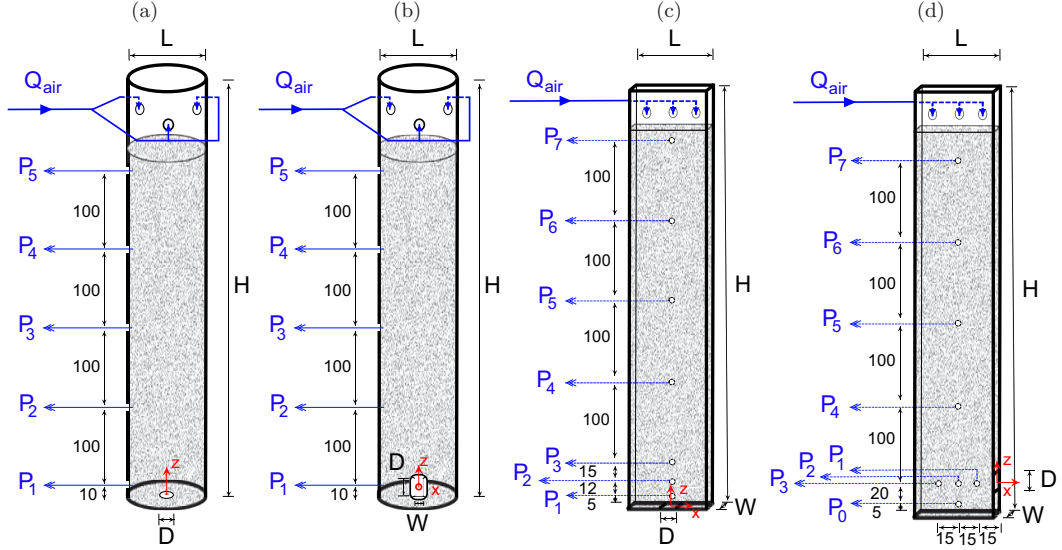


FIG. 1. Sketch of setup with (a) cylindrical silo with orifice at the bottom, (b) cylindrical silo with lateral orifice, (c) rectangular silo with orifice at the bottom, and (d) rectangular silo with lateral orifice. Distances are given in mm. Gravity is aligned with but opposite to the z axis.

constant volumetric flow rate of air Q_{air} , with a relative variation below 10%, through three holes of diameter 4 mm (see Fig. 1). The imposed air flow rate was varied between 1 L/min ($\approx 10^{-5}$ m³/s) and 50 L/min ($\approx 10^{-3}$ m³/s) and was measured during each run using a mass flow meter, Aalborg GFM171009 (range 0–5 L/min) or Aalborg GFM371033 (range 0–50 L/min), with an accuracy of 1% and a response time of 1 s. In order to measure the interstitial air pressure p^f inside the silo, 3 mm holes are drilled at different locations along a median vertical axis, and the other around the orifice, as shown in Fig. 1. These holes are closed with a 40 μm mesh, preventing the particles from going through. Each hole is connected by a tube to one end of a differential piezoelectric pressure sensor, Honeywell DCAL405DN (range ± 1245 Pa) or DCAL430DN (range ± 7472 Pa), with the second end being at the room pressure. The pressure signal was recorded during each run with an accuracy of $\pm 1\%$ and a frequency of 100 Hz.

The granular materials consist of smooth spherical glass beads (density $\rho_p = 2500$ kg/m³, supplied by Potters-Ballotini) with different sizes $d = 124, 190, 375, 538, 762, 1129, \text{ and } 1347$ μm (the uncertainty is evaluated to be $\approx \pm 10\%$).

The experimental procedure is the following: keeping the aperture closed, the glass beads with a total mass m_i were poured in the silo from the top; then the column height (h_p) was measured, giving the initial bulk particle volume fraction $\phi_b = m_i / (\rho_p h_p S_b)$, where S_b is the area of the silo cross section. The top of the silo was then closed. After the preparation phase, the air was injected at a constant flow rate Q_{air} and the orifice of the silo was suddenly opened manually. The beads fall out of the orifice and are collected within a bucket, with the temporal evolution of the mass $m(t)$ being recorded using an electronic balance (Mettler Toledo 6002S) with an accuracy of 0.1 g and a frequency of 20 Hz. One deduces the instantaneous mass flow rate as $Q_i = [m(t + \delta t) - m(t)] / \delta t$, corresponding to the mass of particles falling out of the silo during the time $\delta t = 1$ s.

B. Typical results

In this section, we will first focus on the results obtained in cylindrical silos with a bottom orifice. A typical result is shown in Fig. 2 for $L = 60$ mm, $D = 10$ mm. Figure 2(a) shows the temporal evolution of the instantaneous mass flow rate for a given particle diameter $d = 538$ μm in

TABLE I. Dimensions of the silos (see Fig. 1) and fitting parameters of Eqs. (1), (2), (24), and (25).

Silo	Orifice	Position	L (mm)	H (mm)	D (mm)	W (mm)	C_0	β	α_D	C_{0l}	α_W	γ_2	λ	ξ_ϕ
Cylindrical	Disk	Bottom	20; 40; 60	540	10; 20		0.69	0.08	0.81				1	0.83
Cylindrical	Disk	Lateral	40	540	10; 20; 30			0.08	0.82	0.36			0.27	
Cylindrical	Rectangular	Lateral	20; 40; 60	540	10; 20	5; 10		0.07	0.45	0.49	0.59	1.13	0.27	0.96
Rectangular	Rectangular	Bottom	60	500	10	3.5	0.86	0.08	0.81				1	1
Rectangular	Rectangular	Lateral	60	500	10; 20	3.5		0.19		0.41	0.64	0.56	0.23	1

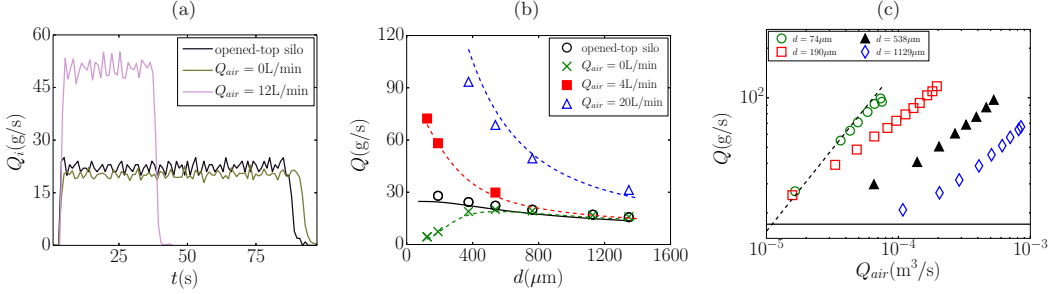


FIG. 2. Cylindrical silo with a bottom orifice with $L = 60$ mm and $D = 10$ mm. (a) Temporal evolution of instantaneous mass flow rate for $d = 538$ μm and different volumetric flow rates of air Q_{air} . (b) Mass flow rate Q vs the particle diameter d for different volumetric flow rates of air Q_{air} . The full line represents Eq. (1) for an opened-top silo. The dashed lines represent the analytical model [Eq. (23)]. (c) Mass flow rate Q vs volumetric flow rate of air Q_{air} for different sizes of particles. The solid line represents the mass flow rate of opened-top silo Q_o with $d = 1129$ μm [Eq. (1)], whereas the dashed line represents Eq. (3).

three conditions: the opened-top silo without influence of air, the closed-top silo without injection of air, and the silo connected to the air injection system with a constant air flow rate $Q_{\text{air}} = 12$ L/min. A steady-state discharge regime is observed in each explored case. The mean flow rate Q is given by the mean value of the instantaneous mass flow rate Q_i during this stationary regime. We can see that the highest value of this flow rate is obtained in the case with a constant air flow rate, demonstrating the strong role of air flow, and the lowest in the case with the closed-top silo, due to a counterflow of air, notably at the orifice, in this configuration. In Fig. 2(b), the mass flow rate is plotted versus the particle diameter d for the opened-top silo and different volumetric flow rate of air, Q_{air} . For the opened-top silo, we recover that the mass flow rate decreases very slightly when increasing the particle diameter. Following [10–12], the data are well fitted by

$$Q_0 = C_0 \phi_b \rho_p [1 - \alpha_D e^{-\beta \frac{D}{d}}] S_0 \sqrt{gD}, \quad (1)$$

with $S_0 = \pi D^2/4$ the orifice area. The fitting parameters C_0 , α_D , and β are given in Table I (see the full line). The dependence with the ratio between the aperture size and the particle diameter D/d can be interpreted as a dilatation at the aperture due to steric effects, where we can note

$$\phi_o = \xi_\phi \phi_b [1 - \alpha_D e^{-\beta \frac{D}{d}}], \quad (2)$$

which is the mean volume fraction at the orifice. The fitting parameter ξ_ϕ is a constant expected to be $\lesssim 1$. It may account for a dilatation due to other effects than the steric effect, as, for example, the shear-rate dependence of the volume fraction observed for dense granular flows [20]. This parameter is included in C_0 and cannot be deduced directly from the measurement of the particle flow rate. With an imposed air flow, the granular flow rate Q becomes all the more sensitive to the air flow rate when the particles size is small as revealed by the relative inclination of the curves in Fig. 2(b). The value of Q is notably impacted by Q_{air} for the case of smaller particles ($d = 190$ μm), whereas for larger particles, Q tends to the asymptotic value Q_0 . The permeability is the main property depending on the particle diameter, which suggests that the coupling between the fluid and the grains is mainly due to the drag force. In Fig. 2(c), the mass flow rate Q is plotted versus the volumetric flow rate of air Q_{air} for different sizes of particles. We observe that the mass flow rate increases with the air flow rate and that it is bounded by two asymptotic behaviors: for small particles, with a very low permeability (dashed line in the figure), the air entering at the top of the silo does not flow throughout the granular media but rather pushes it out of the silo, leading to

$$Q/(\rho_p \phi_b) = Q_{\text{air}}. \quad (3)$$

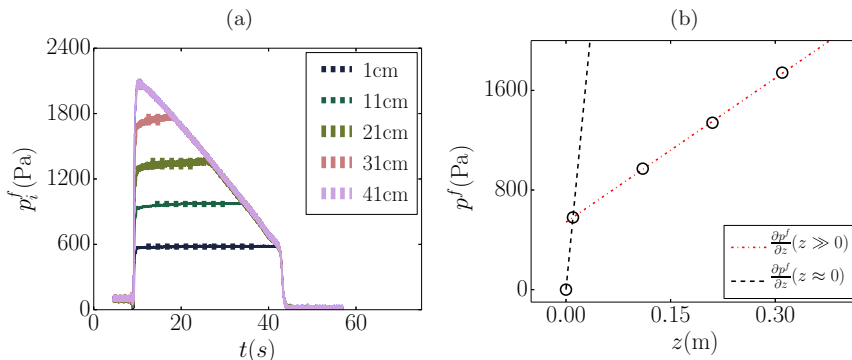


FIG. 3. Cylindrical silo with a bottom orifice with $L = 60$ mm and $D = 10$ mm and $Q_{\text{air}} = 12$ L/min [corresponding to the purple curve in Fig. 2(a)]. (a) Temporal evolution of the instantaneous pressure along the cylindrical silo. (b) Mean pressure in the granular bed along the vertical axis. The black dashed (red dash-dotted) line corresponds to the estimated pressure gradient close to (far from) the orifice. The corresponding equation is $y = 58\,010x$ ($y = 3856x + 541.6$).

For large particles with a very high permeability, and small air flow rate, the air flows easily throughout the granular media and does not affect it, leading to Eq. (1) [see the full line in Fig. 2(c)].

Figure 3(a) shows how the instantaneous pressure of the air along the silo varies with time during the discharge. The room pressure has been subtracted to the signal, such that the reference pressure at the end of the discharge is zero. There is a small overpressure before opening due to the injection of air. During the discharge, a build-up of the pore pressure is observed, corresponding to an air flow through the granular column toward the orifice. For each position, we can see that the pressure exhibits an initial plateau, followed by a quasilinear evolution overlapping other signals. The plateau corresponds to the time during which the sensor is located inside the granular bed. The flow rates and permeability of the granular material being constant, the pressure drop of air between the position of the pressure sensor and the orifice is indeed expected to be constant. Moreover, when the pressure taps are located above the top of the granular bed, with the pressure in this reservoir being uniform, the signals of the sensors are superimposed. The pressure drop is then related to the bed height within the silo, which decreases linearly with time for this stationary discharge. From the plateau, we can deduce the mean air pressure during the discharge, p^f , which we have plotted in Fig. 3(b) as a function of the position along the vertical axis. As expected, we observe that the pressure gradient is constant inside the granular material, except close to the orifice where we observe a much stronger pressure gradient, $(\partial p^f / \partial z)|_{z \approx 0} \approx 15(\partial p^f / \partial z)|_{z \gg 0}$, in the case considered. The orifice surface being smaller than the silo surface, the air velocity and thus the pressure gradient are expected to be higher at the orifice, with a factor $\approx (L/D)^2 \approx 36$ in this case. We recover a lower coefficient than the section ratio for all the configurations studied (varying L and D as summed up in Table I), which seems to suggest that it is not due to the position of the sensor. We rather interpret this observation as an effect of the dilation of the granular media near the orifice which tends to facilitate the air flow by decreasing the permeability and therefore decreasing the local pressure gradient for a given flow rate.

III. TWO-PHASE CONTINUUM MODELING

A. Governing equations and closures

To capture the coupling between the fluid and the granular materials during the discharge of silos, we consider a two-phase continuum model. The mass and momentum conservation equations for

the two phases are given by the following expressions (see [21]):

$$\frac{\partial(1-\phi)}{\partial t} + \frac{\partial((1-\phi)u_i^f)}{\partial x_i} = 0, \quad (4)$$

$$\frac{\partial\phi}{\partial t} + \frac{\partial(\phi u_i^p)}{\partial x_i} = 0, \quad (5)$$

$$\rho_f(1-\phi) \left[\frac{\partial u_i^f}{\partial t} + u_j^f \frac{\partial u_i^f}{\partial x_j} \right] = (1-\phi) \frac{\partial \sigma_{ij}^f}{\partial x_j} - f_i + (1-\phi)\rho_f g_i, \quad (6)$$

$$\rho_p\phi \left[\frac{\partial u_i^p}{\partial t} + u_j^p \frac{\partial u_i^p}{\partial x_j} \right] = \frac{\partial \sigma_{ij}^p}{\partial x_j} + \phi \frac{\partial \sigma_{ij}^f}{\partial x_j} + f_i + \phi\rho_p g_i, \quad (7)$$

where ϕ is the volume fraction of the granular material, u_i^p and u_i^f are, respectively, the local velocities of particles and fluid, and the tensors σ_{ij}^p and σ_{ij}^f are the particle and fluid stress tensors. The term f_i includes the interaction forces between the two phases, beside the buoyancy $\phi\partial\sigma_{ij}^f/\partial x_j$ [21]. Given the range of the particulate Reynolds number, $\text{Re}_p = \rho_f(u^f - u^p)d/\eta_f \lesssim \rho_f Q_{\text{air}}d/(\eta_f D^2) \in [10^{-1} - 10^3]$, we adopt the generalized form that is commonly known as the Forchheimer resistance law (see [22,23]). This law is established for a fixed porous media in which a gas flows and we adapt it using the relative velocity between the two phases:

$$f_i = \frac{\eta_f}{\kappa_v}(1-\phi)^2(u_i^f - u_i^p) + \frac{\rho_f d}{\kappa_i}(1-\phi)^3(u_i^f - u_i^p)|u_i^f - u_i^p|, \quad (8)$$

where, for a granular medium composed of spherical beads, $\kappa_v = \frac{(1-\phi)^3 d^2}{150\phi^2}$ and $\kappa_i = \frac{(1-\phi)^3 d^2}{1.75\phi}$ [24].

To close these equations, we first assume that the viscous stresses in the fluid phase are negligible compared to the drag viscous term, valid as soon as $D^2 \gg \kappa_v$. Under this assumption, the fluid stress tensor simply reduces to the isotropic pressure part, $\sigma_{ij}^f = -p^f \delta_{ij}$. The stress tensor of the particle phase, $\sigma_{ij}^p = -p^p \delta_{ij} + \tau_{ij}^p$, comes only from direct particle-particle interactions and can be described by a shear-dependent frictional rheology [1,20,25]:

$$\tau_{ij}^p = \eta_p(|\dot{\gamma}|, p^p)\dot{\gamma}_{ij} \quad \text{with} \quad \eta_p(|\dot{\gamma}|, p^p) = \frac{\mu(I)p^p}{|\dot{\gamma}|}, \quad I = \frac{|\dot{\gamma}|d}{\sqrt{p^p/\rho_p}}, \quad \text{and} \quad \mu(I) = \mu_s + \frac{\Delta\mu}{I_0/I+1}, \quad (9)$$

where $\dot{\gamma}_{ij} = \partial u_i^p/\partial x_j + \partial u_j^p/\partial x_i$ is the strain-rate tensor with $|\dot{\gamma}| = \sqrt{(\dot{\gamma}_{ij}\dot{\gamma}_{ij}/2)}$ its second invariant, and I_0 , μ_s , and $\Delta\mu$ are constants which depend on the particle's shape and material. We do not take into account the shear-rate dependence of the volume fraction [20]. Finally, in the fluid phase, the flow is taken as stationary and we suppose that the inertial term and the gravity term can be neglected with respect to the drag force [26]. These assumptions are valid as soon as $\rho_f \ll \rho_p$, $D \gg d$ and the Froude number defined on the particle length, $\text{Fr}_p = (u^f - u^p)^2/gd \approx Q_{\text{air}}^2/(gdD^2) \gg \kappa_i d^{-2}$. For convenience, let us introduce a volume-averaged velocity for the mixture as $U_i = \phi u_i^p + (1-\phi)u_i^f$. Given the assumptions above, the two-phase flow obeys

$$\frac{\partial(U_i)}{\partial x_i} = 0, \quad (10)$$

$$-\frac{\partial p^f}{\partial x_i} = \frac{\eta_f}{\kappa_v}(U_i - u_i^p) + \frac{\rho_f d}{\kappa_i}(U_i - u_i^p)|U_i - u_i^p|, \quad (11)$$

$$\frac{\partial\phi}{\partial t} + \frac{\partial(\phi u_i^p)}{\partial x_i} = 0, \quad (12)$$

$$\rho_p\phi \left[\frac{\partial u_i^p}{\partial t} + u_j^p \frac{\partial u_i^p}{\partial x_j} \right] = \frac{\partial \sigma_{ij}^p}{\partial x_j} - \frac{\partial p^f}{\partial x_i} + \phi\rho_p g_i. \quad (13)$$

This system of equations describes the discharge flow of a granular medium interacting with a moving gas.

B. Numerical implementation in a simplified configuration

To study the effect of the air injection on the discharge flow of the silo, we numerically solved Eqs. (10)–(13) in a simplified configuration where we focus on the viscous regime for the interstitial flow of air ($\kappa_i = \infty$). We consider a two-dimensional silo of width L and height $H = 4L$ with an orifice of dimension D at the center of the bottom of the silo, initially filled with a height $h_p = 3.9L$ of the viscoplastic fluid. The mesh is such that the width of the silo L is divided in 64 computation cells, which is a good balance between precision and computational time. Following [6] to take into account the lateral friction on the walls, which is supposed to be a Coulomb force $-\mu_w p^p$ on each wall, we average the momentum equation [Eq. (13)] across the thickness of the silo:

$$\rho \left[\frac{\partial u_i^p}{\partial t} + u_j^p \frac{\partial u_i^p}{\partial x_j} \right] = \frac{\partial \sigma_{ij}^p}{\partial x_j} - \frac{\partial p^f}{\partial x_i} + \rho g_i + f_{wi} \quad \text{with} \quad f_{wi} = -2 \frac{\mu_w p^p}{W} \frac{u_i^p}{|u_i^p|}, \quad (14)$$

where the effective density of the granular media, $\rho = \phi \rho_p$, is taken constant, $= \rho_p$, for simplicity. Indeed, we do not consider the variation of the volume fraction with I given by [20], as we suppose the granular flow to be incompressible. We solve Eq. (14) made dimensionless using L as a length scale, $\rho g L$ as a pressure scale, $\sqrt{L/g}$ as a timescale, and, following Staron *et al.* [27], we take, for the rheological constants, $\mu_s = 0.4$, $\Delta\mu = 0.28$, $I_0 = 0.4$, and $\mu_w = 0.1$. Moreover, we use a regularization technique to avoid the divergence of the viscosity when the shear becomes too small by replacing η_p by $\min(\eta_p, \eta_{\max})$, with $\eta_{\max} = 100\rho\sqrt{gL^3}$ a constant that is large enough [2,3,6,27]. Concerning the fluid phase, combining the momentum conservation [Eq. (11)] with the mass conservation [Eqs. (10) and (12)], we obtain

$$\frac{\partial}{\partial x_i} \left(\zeta \frac{\partial p^f}{\partial x_i} \right) = 0, \quad (15)$$

where $\zeta = \kappa_v \rho \sqrt{g/L} / \eta_f$ is the dimensionless permeability considered constant across the silo. The Navier-Stokes simulations are performed with the free software BASILISK [28], which uses a finite-volume projection method. Two phases are present: a surrounding passive gas for $z > h_p$ with a small density, a small viscosity, and a very high permeability $\zeta_\infty = 100 \gg 1$, and the granular media for $z \leq h_p$, where $\zeta = 1$. At each time step, we first solve Eq. (15), corresponding to a Poisson-Helmholtz equation, using a specific solver [29,30]. We consider a Dirichlet condition at the orifice ($p^f = 0$) and a Neumann condition at the solid boundaries ($n_i \partial p^f / \partial x_i = 0$), where n_i is the vector unity normal to the surface. To simulate the air injection at the top of the silo, we suppose that far from the orifice, the flows are uniform, $U_z(h_p) = Q_{\text{air}}/L$ and $u_z^p(h_p) = Q_i/\rho L$, leading to the boundary condition at the top of the domain,

$$\frac{\partial p^f}{\partial z} \Big|_{z=H} = - \frac{(Q_{\text{air}} - Q_i/\rho)}{\zeta_\infty L} \rho \sqrt{g/L}. \quad (16)$$

This condition couples the flows of the two phases. It depends on the instantaneous particle flow rate Q_i , which is computed at each time step. The resolution of Eq. (15) gives the fluid pressure field p^f and its gradients, corresponding to the fluid-particle coupling in Eq. (14), which can then be solved with a no-slip condition at the solid boundaries and a zero particle pressure at the orifice and at the top boundary of the domain. Finally, the interface between these two phases is tracked with a volume-of-fluid method; see [2,3,6,27] for more details.

We performed a set of simulations for $L = 90d$, $D = 0.25L$, and $W = 0.25L$, where we varied the air flow rate Q_{air} . Figure 4(a) shows the temporal evolution of the dimensionless instantaneous mass flow rate $Q_i/(\rho_p \sqrt{gL^3})$ in three conditions: no coupling with the fluid phase, equivalent to the opened-top silo, or coupling with the fluid phase, equivalent to the closed-top silo, with $Q_{\text{air}} = 0$

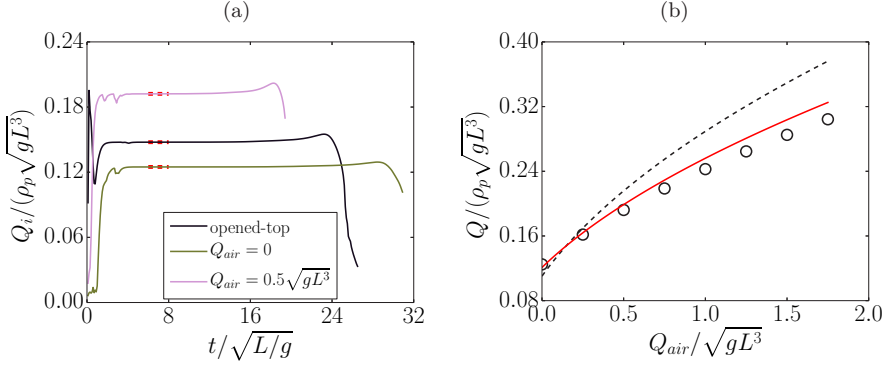


FIG. 4. Continuum simulation of the discharge of a silo with orifice at the bottom for $L = 90d$, $D = 0.25L$, and $W = 0.25L$. (a) Temporal evolution of the dimensionless instantaneous flow rate $Q_i / (\rho_p \sqrt{gL^3})$ as a function of the dimensionless time $t / \sqrt{L/g}$. (b) $Q / \rho_p \sqrt{gL^3}$ as a function of $Q_{air} / \sqrt{gL^3}$. The lines represent the simple analytical model [Eq. (23)] with $A = 1$ (black dashed line) and $A = 0.68$ (red line).

(no injection of air) and $Q_{air} = 0.5\sqrt{gL^3}$. Similarly to the experiment, we observe a steady-state discharge regime in each explored case and we recover that the highest value of the mean flow rate is obtained in the case with a constant air flow rate, and the lowest in the case with the closed-top silo ($Q_{air} = 0$). In Fig. 4(b), the dimensionless mass flow rate $Q / (\rho_p \sqrt{gL^3})$ is found to increase with the dimensionless volumetric flow rate of air $Q_{air} / \sqrt{gL^3}$, as in the experiments. Following the experimental measures, Fig. 5(a) shows the temporal variation of the instantaneous air pressure along the silo. We observe the same behavior as in the experiments, with a build-up of the pore pressure, and for each position a plateau followed by a linear evolution where all the signals are finally superimposed. In Fig. 5(b), we have plotted the mean air pressure p^f deduced from the plateau, as a function of the position along the vertical axis. We observe a constant pressure gradient far from the orifice and a stronger pressure gradient close to the orifice, $(\partial p^f / \partial z)|_{z \approx 0} = (L/D)(\partial p^f / \partial z)|_{z \gg 0}$, exactly due to the change in the air flow area; indeed, in the

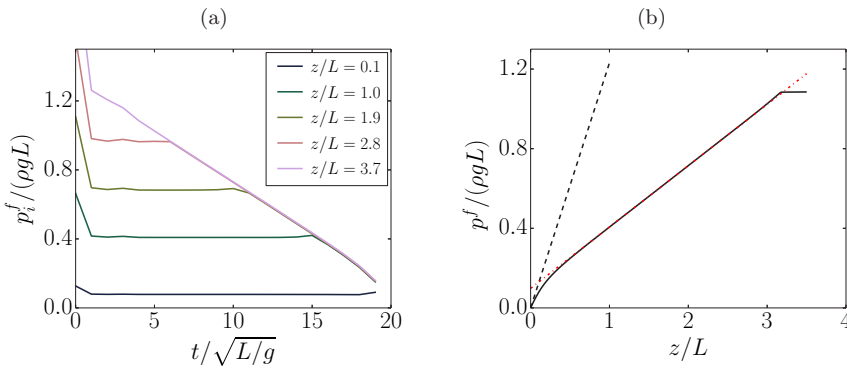


FIG. 5. Continuum simulation with orifice at the bottom for $L = 90d$, $D = 0.25L$, $W = 0.25L$, and $Q_{air} / \sqrt{gL^3} = 0.5$ [corresponding to black line in Fig. 4(a)]. (a) Pressure $p^f / \rho g L$ along the center of the silo vs time $t / \sqrt{L/g}$ for different positions. (b) Mean pressure in the granular bed along the vertical axis. The black dashed line corresponds to a linear adjustment of the pressure close to the orifice with $y = \frac{\eta \beta L}{S_o} (Q_{air} - Q / \rho_p)x = 1.23x$. The red dash-dotted line corresponds to a linear adjustment of the pressure far from the orifice with $y = \frac{\eta \beta L}{S_o} (Q_{air} - Q / \rho_p)x + 0.098 = 0.308x + 0.098$, where the numerical parameter is obtained using the least-squares method.

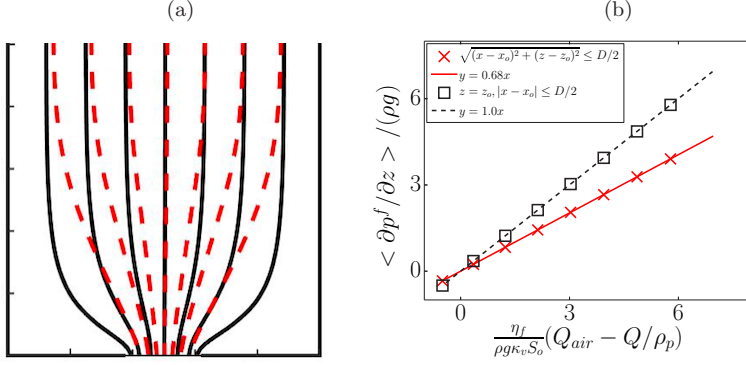


FIG. 6. Continuum simulation of discharge of a silo with an orifice at the bottom for $L = 90d$, $D = 0.25L$, $W = 0.25L$, and $Q_{\text{air}}/\sqrt{gL^3} = 0.5$ [corresponding to the black line in Fig. 4(a)]. (a) Streamlines for the particle phase (red dashed lines) and for the fluid phase (black full lines). (b) Air mean pressure gradient $\langle \partial p^f / \partial z \rangle$ averaged along the orifice (□) and in the accelerated zone near the orifice (×) vs $\frac{\eta_f}{\rho g \kappa_v S_0} (Q_{\text{air}} - Q / \rho_p)$. The dashed (full) line corresponds to the best linear fit.

simulation, the volume fraction is kept constant. The transition between the two zones then occurs for $z \approx 0.42D$. Using the results of this simulation, in the next section we propose an analytical model to predict the flow rate of the discharge of a granular media from silos with injection of air.

IV. AN ANALYTICAL MODEL

A. Hypothesis of the model and numerical validation

We have seen in Secs. II B and III B that the air flow strongly influences the discharge rate of the silo. As already shown in other flow configurations [17–19] and suggested by the conservation of the momentum of the particle phase [Eq. (13)], the air-pressure gradient acts as a driving force in addition to gravity. With the silo discharge controlled by the flow at the orifice [8–10,31], following the models proposed in [17–19], we consider that the variation of the granular flow due to air flow can be modeled as a modification of the driving force. Therefore, the particle mass flow rate in the presence of a fluid pressure gradient, issued from Eq. (1) with a correction of gravity, reads

$$Q = Q_0 \left(1 + \frac{1}{\phi_o \rho_p g} n_i \left. \frac{\partial p^f}{\partial x_i} \right|_o \right)^{1/2}, \quad (17)$$

where Q_0 is the opened-top silo case flow rate, $n_i \left. \frac{\partial p^f}{\partial x_i} \right|_o$ is the air-pressure gradient normal to the orifice (i.e., $\partial p^f / \partial z|_o$ for a bottom orifice), and ϕ_o is the volumetric fraction of particles, both near the orifice. The fluid pressure gradient depends on the position in the silo and is given by the momentum balance for the fluid phase [Eq. (11)].

The simulations result [see Fig. 6(a)] supports the assumption of quasivertical streamlines close to the orifice. Given the constant volumetric air flow rate imposed at the top of the silo Q_{air} and the corresponding steady particle mass flow rate at the orifice Q , the local relative velocity between the mixture and particles at the orifice, $v_{\text{rel}} = n_i [U_i(0) - u_i^p(0)]$, can be deduced from a mass balance across the silo assuming incompressibility:

$$v_{\text{rel}} = \frac{Q_{\text{air}} - Q / (\phi_o \rho_p)}{S_0}, \quad (18)$$

where S_0 is the orifice cross section. The singular value $Q_{\text{air}} = Q / (\phi_o \rho_p)$ exactly compensates the volumetric granular flux similarly to an opened-top case silo with $v_{\text{rel}} = 0$ and $Q = Q_0$. For lower

air flow rates at the top of the silo, there is a counterflow of air at the orifice. It leads to the observed values of Q less than Q_0 for the smallest particle size and very low values of Q_{air} . For the sake of clarity, we introduce the nondimensional flow rates relative to the discharge rate in the absence of fluid interaction Q_0 , i.e., for the granular flow rate $\bar{Q} = \frac{Q}{Q_0}$ and for the air flow rate $\tilde{Q} = \frac{\phi_0 \rho_p Q_{\text{air}}}{Q_0}$, as well as the notation

$$\pm = \frac{\tilde{Q} - 1}{|\tilde{Q} - 1|} = \frac{v_{\text{rel}}}{|v_{\text{rel}}|} = -\mp, \quad (19)$$

whose values are $+1$ in the case of cocurrent flow and -1 in the case of countercurrent flow. Let us assume that the air-pressure gradient is nearly uniform in the orifice region. This leads to [from Eq. (11)]

$$n_i \frac{\partial p^f}{\partial x_i} \Big|_o \approx \pm \left[\frac{\eta_f}{\kappa_v(\phi_o, d)} |v_{\text{rel}}| + \frac{\rho_f d}{\kappa_i(\phi_o, d)} |v_{\text{rel}}|^2 \right]. \quad (20)$$

Figure 6(b) shows that for the continuum simulation in the Darcy flow case ($\kappa_i^{-1} = 0$), the mean air-pressure gradient averaged at the orifice (\square) is well represented by Eq. (20) (black dashed line). Combining Eqs. (17), (18), and (20) provides a direct relation between \bar{Q} and \tilde{Q} and, after rather simple calculations, we get

$$(1 \mp \mathcal{N}_i) \bar{Q}^2 + (\mathcal{N}_v \pm 2\mathcal{N}_i \tilde{Q}) \bar{Q} - (1 + \mathcal{N}_v \tilde{Q} \pm \mathcal{N}_i \tilde{Q}^2) = 0, \quad (21)$$

where we introduced

$$\mathcal{N}_v = \frac{\eta_f Q_0}{\phi_o^2 \rho_p^2 \kappa_v(\phi_o, d) g S_0} \quad \text{and} \quad \mathcal{N}_i = \frac{\rho_f d Q_0^2}{\phi_o^3 \rho_p^3 \kappa_i(\phi_o, d) g S_0^2}. \quad (22)$$

For a given air flow rate and system dimensions (say \tilde{Q} , \mathcal{N}_v , and \mathcal{N}_i), Eq. (21) is a quadratic equation for \bar{Q} . Its single positive root is the solution of our problem (the discriminant Δ is always strictly positive and therefore there are always two roots and the second root, which is negative, that would correspond to particles entering the silo has no physical meaning in our context) and reads

$$\bar{Q} = \frac{(\mp 2\mathcal{N}_i \tilde{Q} - \mathcal{N}_v) + \sqrt{\Delta}}{2(1 \mp \mathcal{N}_i)} \quad \text{with} \quad \Delta = \mathcal{N}_v^2 + 4(1 + \mathcal{N}_v \tilde{Q}) \pm 4\mathcal{N}_i(\tilde{Q}^2 - 1). \quad (23)$$

The trivial solution $\bar{Q} = 1$ when $\tilde{Q} = 1$ is recovered for any value of \mathcal{N}_v or \mathcal{N}_i . The asymptotic limit at large values of fluid-particle inertia dominated drag ($\mathcal{N}_i \rightarrow +\infty$) corresponds to the solution $\bar{Q} = \tilde{Q}$: the air entering at the top of the silo does not flow throughout the granular media, but rather pushes it out of the silo. In Fig. 4(b), we compare the numerical simulation results with Eq. (23) (black dashed line) for the Darcy flow case $\mathcal{N}_i = 0$. We observe that Eq. (23) overpredicts the flow rate. This suggests that the mean air-pressure gradient near the orifice needs to be evaluated on a larger zone (where it should necessarily be lower). In Fig. 6(b), we calculate the mean air-pressure gradient ($\partial p^f / \partial z$) averaged on a circular zone of size $D/2$ above the orifice (\times), corresponding roughly to the zone where the particles accelerate [8,31]. We observe that ($\partial p^f / \partial z$) is still proportional to $\eta_f |v_r| / \kappa_v$, as supposed in Eq. (20), but with a coefficient $\mathcal{A} = 0.68$, lower than 1 due to the two-dimensional (2D) flow in this zone (red full line). This implies that the model given in Eq. (23) should still be valid if replacing \mathcal{N}_v by $\mathcal{A}\mathcal{N}_v$. This corresponds to the red full line of Fig. 4(b), which gives a good prediction of the flow rate.

B. Comparison with experiments

In contrast with the numerical simulation, in the experiment the granular medium tends to dilate at the orifice. In the presence of air flow, this dilation also impacts the permeability of the granular phase in the near orifice region, which suggests that Eq. (20) represents the mean pressure gradient in the region where the particle are accelerated, considering that ϕ_o represents the volume fraction in

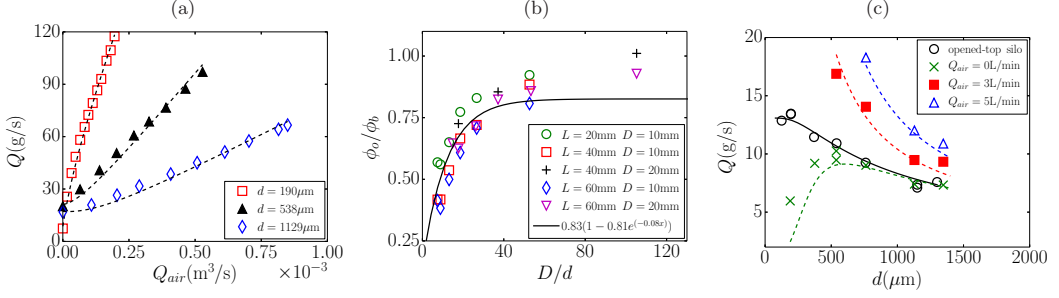


FIG. 7. Silo with orifice at the bottom. (a) Mass flow rate of particles vs volume flow rate of air Q_{air} for the cylindrical silo with $L = 60$ mm, $D = 10$ mm for different sizes of particles. The dashed lines represent Eq. (23) with the adjusted parameter ϕ_o by using the least-squares method. (b) ϕ_o/ϕ_b vs D/d , with different sizes of L and D , where the solid line represents Eq. (2) with the fitting parameters given in Table I. (c) Mass flow rate vs different sizes of particles d for different volume flow rates of air Q_{air} for the rectangular silo with $L = 60$ mm, $D = 10$ mm, and $W = 3.5$ mm. The full line represents Eq. (1) for an opened-top silo. The dashed lines represent Eq. (23) with the fitting parameters given in Table I.

this region. To test this hypothesis, we deduce ϕ_o as an adjusted parameter of the model [Eq. (23)] to fit the data of the mass flow rate of particles versus the volume flow rate of air [Fig. 7(a)]. In Fig. 7(b), we have plotted the obtained value of ϕ_o , normalized by ϕ_b as a function of the dimensionless aperture size D/d , for different silo diameters L and aperture diameters D . We observe that the data superimpose in this representation and are well represented by Eq. (2) (see the full line in the figure), where for simplicity we use the coefficients α and β obtained previously for the opened-top silo [Eq. (1)] supposing that the steric effect is scarcely influenced by the air flow. The fitting parameter ξ_ϕ , given in Table I, will then also account for the zone of evaluation of the pressure gradient, similarly to \mathcal{A} in the numerical simulation.

Finally, once supplemented by a law for Q_0 and ϕ_o given, respectively, by Eqs. (1) and (2), which rely on four fitting parameters, i.e., C_0 , ξ_ϕ , α , and β , the model [Eq. (23)] is found to be predictive; see the dashed lines in Fig. 2(b). This model is also valid for a rectangular silo with a bottom orifice, as can be seen in Fig. 7(c), where the agreement with the experimental data is fairly good, with the fitting parameters given in Table I.

V. VALIDATION OF THE ANALYTICAL MODEL FOR A LATERAL ORIFICE

We can generalize the analytical model to silos with a lateral orifice [see Figs. 1(b) and 1(d)]. In this configuration, Zhou *et al.* have shown that the flow rate of an opened-top silo is modified [6]. They proposed an empirical law to predict the flow rate for a lateral orifice of thickness W and height D ,

$$Q_{ol} = C_{ol} \rho \phi_b G_D \left(\frac{D}{d} \right) G_W \left(\frac{W}{d} \right) F \left(\frac{D}{W} \right) W \sqrt{gD^3}. \quad (24)$$

The function $F(D/W) = [1 + \gamma_2 D/W]^{-1/2}$ accounts for the effect of the friction on the lateral wall, which tends to align the velocity with gravity when the thickness decreases and, consequently, reduces the flow rate. The geometrical functions $G_D(D/d) = [1 - \alpha_D e^{-\beta \frac{D}{d}}]$ and $G_W(W/d) = [1 - \alpha_W e^{-\beta \frac{W}{d}}]$ account for the dilation at the aperture due to steric effects,

$$\phi_{ol} = \xi_\phi \phi_b G_D \left(\frac{D}{d} \right) G_W \left(\frac{W}{d} \right). \quad (25)$$

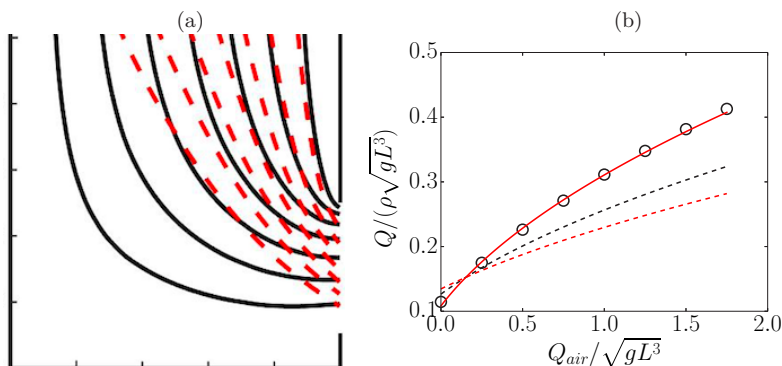


FIG. 8. Continuum numerical simulation for a silo with a lateral orifice with $D = 0.40625L$ and $W = 0.25L$. (a) Streamlines for the granular flow (red dashed line) and for the air flow (black lines). (b) $Q/\rho\sqrt{gL^3}$ as a function of $Q_{air}/\sqrt{gL^3}$. The lines represent Eq. (23) with $A = 1$ and $\lambda = 1$ (---), $A = 0.67$ and $\lambda = 1$ (---), and $A = 0.67$ and $\lambda = 0.36$ (—).

The fitting parameters of Eq. (24) have been obtained in the opened-top silo [see the full line in Figs. 9(a) and 9(b)] and are summed up in Table I, where we consider, for the rectangular silo, that $G_D(D/d) \approx 1$.

Figure 8(a) shows the streamline of the granular media (dashed red lines) and of the air (black lines) obtained numerically in the laminar regime. Even though the orifice normal is orthogonal to the direction of gravity, the latter still drives the discharge. The difference between the two configurations (orifice at the bottom or lateral) reduces to the different values of the empirical constants, namely, C_0 for the bottom case and C_{0l} for the lateral case. Therefore, for the same shape of a large orifice ($D/d \gg 1$) in the Hagen-Beverloo regime ($D/W \ll 1$), the ratio $\lambda = (C_{0l}/C_0)^2 < 1$ can be related to a reduction of the driving force in the lateral case that then reads λg . Thus, the previous approach and Eq. (23) should still be valid in the lateral case if we keep the empirical constants from the bottom case but replace g by λg .

Figure 8(b) shows the comparison between the continuum numerical simulations in the viscous regime and the analytical model for several A and λ values. Both corrective coefficients A (which account for the zone of evaluation of the pressure gradient) and λ are necessary to fit the data.

Finally, Fig. 9 compares the experimental results for a lateral orifice, and for the cylindrical and the rectangular silos, with the generalized model given by Eq. (23) with the reduced gravity λg and the adjusted parameters given in Table I. The coefficient ξ_ϕ has been adjusted to the data following the previous approach. We observe that the agreement is fairly good for both the cylindrical and rectangular silos.

VI. CONCLUSION

Using experiments and continuum simulations, we have studied the effect of injection of a constant flow rate of air in the discharge of a silo with a bottom or a lateral orifice. Steady flow regimes are obtained. We observe that the particle flow rate increases with the air flow rate and decreases with the particle size. Based on a continuum two-phase model using a frictional rheology for the particulate phase, we propose an analytical model where the fluid pressure gradient near the orifice acts as an additional driving force with respect to gravity, in accordance with previous authors [17–19]. This model is validated by the continuum simulations, where we observe that the driving fluid pressure gradient corresponds to a mean gradient on a circular zone of size $D/2$ above the orifice where the particles accelerate [8,31].

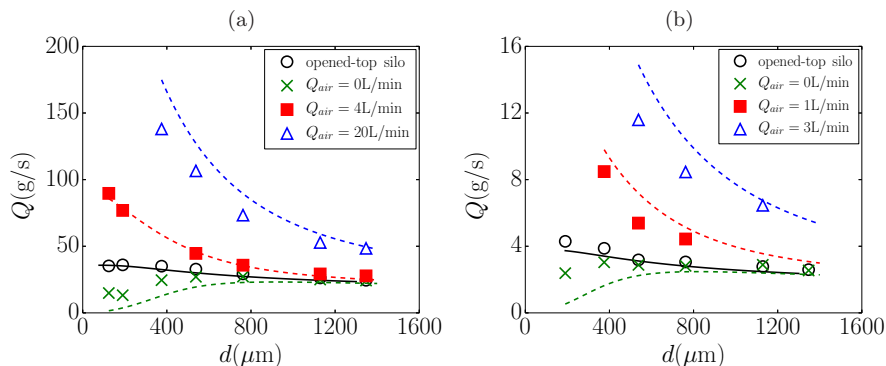


FIG. 9. Mass flow rate vs size of particles d for different volume flow rates of air Q_{air} , for lateral orifices. (a) Cylindrical silo with $L = 60$ mm, $D = 20$ mm, and $W = 10$ mm. (b) Rectangular silo with $L = 60$ mm, $D = 10$ mm, and $W = 3.5$ mm. The full lines represent Eq. (24) and the dashed lines represent the generalized model (23), with the adjusted parameters given in Table I.

The permeability variation at the orifice, associated with dilation of the granular medium that accelerates, is accounted for thanks to a function of the dimensionless aperture size (D/d). The analytical model includes four fitting parameters, which can be obtained with a first series of experiments with an opened-top silo, varying either the orifice size or the particle size (giving C_0 , α , and β), and a second series of experiments varying the air flow rate for a large ratio between the aperture size and the particles diameter (giving ξ_ϕ). To take into account the position of the orifice, the driving force for an opened-top silo needs to be modified (g needs to be replaced with λg) to take into account the inclination of the granular medium streamlines. This parameter is obtained with a series of experiments with an opened-top silo with a lateral orifice varying either the orifice size or the particle size. We finally obtain a fairly good agreement between the analytical model and the experiments. It would be good in the future to test configurations where the particle's shape or polydispersity in size are varied or where the particle and air flows are nonstationary, as can be seen in industrial situations.

ACKNOWLEDGMENTS

We would like to thank P. Cervetti, S. Noel, and F. Ratouchniak for technical assistance. This work is funded by the Institut de Radioprotection et de Sûreté Nucléaire (IRSN) and Électricité de France (EDF) in the framework of their collaborative research programs. It has been carried out in the framework of the Labex MEC and of the Excellence Initiative of Aix-Marseille University - A*MIDEX project, a French “Investissements d’Avenir” programme. Y.Z. thanks the National Natural Science Foundation of China for support (Grant No. 11802094).

-
- [1] P. Jop, Y. Forterre, and O. Pouliquen, A constitutive law for dense granular flows, *Nature (London)* **441**, 727 (2006).
 - [2] P.-Y. Lagr e, L. Staron, and S. Popinet, The granular column collapse as a continuum: Validity of a two-dimensional Navier-Stokes model with a $\mu(I)$ -rheology, *J. Fluid Mech.* **686**, 378 (2011).
 - [3] L. Staron, P.-Y. Lagr e, and S. Popinet, Continuum simulation of the discharge of the granular silo, *Eur. Phys. J. E* **37**, 5 (2014).
 - [4] S. Dunatunga and K. Kamrin, Continuum modeling and simulation of granular flows through their many phases, *J. Fluid Mech.* **779**, 483 (2015).

- [5] G. Davier and F. Bertails-Descoubes, Nonsmooth simulation of dense granular flows with pressure-dependent yield stress, *J. Non-Newton Fluid Mech.* **234**, 15 (2016).
- [6] Y. Zhou, P. Y. Lagr e, S. Popinet, P. Ruyer, and P. Aussillous, Experiments on, and discrete and continuum simulations of, the discharge of granular media from silos with a lateral orifice, *J. Fluid Mech.* **829**, 459 (2017).
- [7] M. Ishikawa and S. Shiozawa, A study of fuel behavior under reactivity initiated accident conditions - Review, *J. Nucl. Mater.* **95**, 1 (1980).
- [8] B. P. Tighe and M. Sperl, Pressure and motion of dry sand: Translation of Hagen's paper from 1852, *Granul. Matt.* **9**, 141 (2007).
- [9] W. A. Beverloo, H. A. Leniger, and J. Van de Velde, The flow of granular solids through orifices, *Chem. Eng. Sci.* **15**, 260 (1961).
- [10] A. Janda, I. Zuriguel, and D. Maza, Flow Rate of Particles Through Apertures Obtained from Self-Similar Density and Velocity Profiles, *Phys. Rev. Lett.* **108**, 248001 (2012).
- [11] M. Benyamine, M. Djermane, B. Dalloz-Dubrujeaud, and P. Aussillous, Discharge flow of a bidisperse granular media from a silo, *Phys. Rev. E* **90**, 032201 (2014).
- [12] Y. Zhou, P. Ruyer, and P. Aussillous, Discharge flow of a bidisperse granular media from a silo: Discrete particle simulations, *Phys. Rev. E* **92**, 062204 (2015).
- [13] R. A. Altenkirch and R. Eichhorn, Effect of fluid drag on low Reynolds number discharge of solids from a circular orifice, *AIChE J.* **27**, 593 (1981).
- [14] B. J. Crewdson, A. L. Ormond, and R. M. Nedderman, Air-impeded discharge of fine particles from a hopper, *Powder Technol.* **16**, 197 (1977).
- [15] S.-S. Hsiau, C.-C. Hsu, and J. Smid, The discharge of fine silica sands in a silo, *Phys. Fluids* **22**, 043306 (2010).
- [16] J. E. Hilton and P. W. Cleary, Granular flow during hopper discharge, *Phys. Rev. E* **84**, 011307 (2011).
- [17] J. A. H. de Jong, Vertical air-controlled particle flow from a bunker through circular orifices, *Powder Technol.* **3**, 279 (1969).
- [18] J. A. H. de Jong and Q. E. J. J. M. Hoelen, Cocurrent gas and particle flow during pneumatic discharge from a bunker through an orifice, *Powder Technol.* **12**, 201 (1975).
- [19] R. M. Nedderman, U. T z n, and R. B. Thorpe, The effect of interstitial air pressure gradients on the discharge from bins, *Powder Technol.* **35**, 69 (1983).
- [20] Y. Forterre and O. Pouliquen, Flows of dense granular media, *Annu. Rev. Fluid Mech.* **40**, 1 (2008).
- [21] R. Jackson, *The Dynamics of Fluidized Particles* (Cambridge University Press, Cambridge, 2000).
- [22] S. Whitaker, The Forchheimer equation: A theoretical development, *Transp. Porous Med.* **25**, 27 (1996).
- [23] J. L. Lage, The fundamental theory of flow through permeable media from Darcy to turbulence, in *Transport Phenomena in Porous Media*, edited by Derek B. Ingham and Iacono Pop (Pergamon, Oxford, 1998), pp. 1–30.
- [24] S. Ergun, Fluid flow through packed columns, *Chem. Eng. Prog.* **48**, 89 (1952).
- [25] G. D. R. Midi, On dense granular flows, *Eur. Phys. J. E* **14**, 341 (2004).
- [26] D. A. Nield and A. Bejan, *Convection in Porous Media* (Springer, New York, 2006).
- [27] L. Staron, P.-Y. Lagr e, and S. Popinet, The granular silo as a continuum plastic flow: The hour-glass vs the clepsydra, *Phys. Fluids* **24**, 103301 (2012).
- [28] S. Popinet, Basilisk C reference manual, http://basilisk.fr/Basilisk_C (unpublished).
- [29] Poisson-Helmholtz equation solver, <http://basilisk.fr/src/poisson.h#multigrid-poissonhelmholtz-solvers> (unpublished).
- [30] S. Popinet, A quadtree-adaptive multigrid solver for the Serre-Green-Naghdi equations, *J. Comput. Phys.* **302**, 336 (2015).
- [31] S. M. Rubio-Largo, A. Janda, D. Maza, I. Zuriguel, and R. C. Hidalgo, Disentangling the Free-Fall Arch Paradox in Silo Discharge, *Phys. Rev. Lett.* **114**, 238002 (2015).